Sound & Vibration 2026, 60(1), 3786.
doi: https://doi.org/10.59400/sv3786

Article

A low-frequency sound absorption structure easily manufactured by machine for transformer noise

Ke Xu[1], Kanyu Wang[1], Qinhao Lin[2], Guoqing Di[1,3,*]

[1] College of Environmental and Resource Sciences, Zhejiang University, Hangzhou 310058, China
[2] Yangtze Delta Region Institute (Huzhou), University of Electronic Science and Technology of China, Huzhou 313001, China
[3] Innovation Center of Yangtze River Delta, Zhejiang University, Jiaxing 314102, China
*** Corresponding author:** Guoqing Di, dgq@zju.edu.cn

CITATION

Xu K, Wang K, Lin Q, et al. A low-frequency sound absorption structure easily manufactured by machine for transformer noise. Sound & Vibration. 2026; 60(1): 3786. https://doi.org/10.59400/sv3786

ARTICLE INFO

Received: 27 August 2025
Revised: 29 September 2025
Accepted: 12 October 2025
Available online: 6 January 2026

Abstract: Many tonal noises in the environment have a high annoyance. It is necessary to develop acoustic materials for targeted absorption of tonal noise in order to reduce its impact. As the primary noise source in substations, transformers emit low-frequency noise with distinct tonal characteristics. According to basic constraints of materials in substations, such as fire resistance, weather resistance, and ease of machine manufacturing, a sound absorption structure (SAS) is developed for the absorption of noise from 110 kV transformers in this study. SAS is an aluminum alloy flat plate tiled with repeatable basic sound absorption units. Each basic unit consists of two vertically stacked Helmholtz resonators, both of which have an inserted duct. The acoustic performance of SAS is studied by theoretical analysis, numerical simulation, and experimental measurement. Analysis results showed that ratios of its surface acoustic impedance to air acoustic impedance at two resonant frequencies of 100 Hz and 200 Hz were close to 1. Measurement results indicated that sound absorption coefficients respectively reached 0.93 and 0.90 in the normal incident sound field, and reached 0.83 and 0.88 in the diffuse sound field. Moreover, the fire resistance grade of SAS reached the A1 level, which indicated it was completely non-combustible. Laying SAS on reflective surfaces of structures, such as transformer firewalls, can reduce the impact of low-frequency noise.

Keywords: low-frequency; tonal noise; sound absorption materials; acoustic metamaterials; transformer noise

1. Introduction

Tonal noise refers to noise with one or several tones, and its sound energy is mainly concentrated at one or several specific frequencies. Tonal noise is produced by many common sources, including transformers [1], air conditioning compressors [2], propellers [3], wind turbines [4], and liquid-filled pipelines [5]. At the same A-weighted equivalent sound pressure level, tonal noise is typically rated as more annoying than atonal noise [2, 6, 7]. Reducing noise at the source is often effective to mitigate impacts, but it can compromise equipment performance [8,9]. Active noise control (ANC) technology can effectively control single-frequency or narrowband noise in small enclosed spaces [5,10], but its noise reduction effect is not ideal in large or open spaces [11, 12]. Therefore, from the perspective of sound propagation paths, passive noise reduction technology for the control of tonal noise remains one of the more practical solutions [13].

At the interested frequencies, the received sound includes direct sound radiated by the source and reflected sound from nearby surfaces. Laying acoustic materials that absorb tonal noise on reflection surfaces can reduce the impact of tonal noise [14]. Common sound absorption materials include porous sound absorption materials [15,16] and resonant sound absorption structures [17]. Porous materials can be used to absorb broadband noise with medium and high frequency components, but they provide limited absorption at low frequencies [18,19]. Resonant sound absorption structures can absorb tonal noise with medium and low frequency components, but their size is relatively large due to the constraint of the causal law [20]. In practical application scenarios, in addition to acoustic performance, sound absorption materials also need to meet non-acoustic performance requirements such as fire resistance, weather resistance, and ease of machine manufacturing. Therefore, an urgent problem in the development of high-performance sound absorption materials is how to break through the causal law and construct a universal acoustic structure that can absorb tonal noise of low-frequency based on constraint conditions (e.g., requirements of non-acoustic performance for different application scenarios). To improve sound absorption performance, it is theoretically feasible to introduce complex sound absorption structures and produce physical objects through 3D-printing. However, in practice, due to high manufacturing costs, it cannot be applied in engineering.

This study took a 110 kV transformer noise with significant low-frequency tonalities as an example, regarded materials' fire resistance, weather resistance, and ease of machine manufacturing as basic constraints, and constructed a low-frequency sound absorption structure. Its acoustic performance and mechanism were studied by theoretical analysis, numerical simulation, and experimental measurement.

2. Structure and theory

2.1. Design of sound absorption structure (SAS)

In China, the power system uses alternating current of 50 Hz. Due to the magnetostriction of the transformer core which happens twice per current cycle, the radiated sound energy of transformers is mainly concentrated at the second and fourth harmonics of 50 Hz [6,21]. A typical noise spectrum of a 110 kV transformer is shown in **Figure 1**. As shown in **Figure 1**, sound energy at 100 Hz and 200 Hz dominates transformer noise, which is consistent with the result of studies by Li et al. [6] and Sharafkhani [21]. Materials in substations must meet strict fire resistance requirements. For example, the fire resistance grade of transformer firewalls must reach A1 level (completely non-combustible) as specified in EN 13501-1:2007. Aluminum alloy has a high fire resistance grade, excellent mechanical properties, and is easy to process and shape. Thus, it was used to construct SAS in this study.

As shown in **Figure 2**, the structure of SAS was designed for the targeted absorption of sound energy of the interested frequencies. SAS is composed of square sound absorption boxes arranged periodically (see **Figure 2a**). Each square sound absorption box contains four basic units. Each basic unit consists of two Helmholtz resonators stacked vertically, and each Helmholtz resonator is equipped with an inserted duct.

Figure 2b shows the assembly diagram of the square sound absorption box. As shown in **Figure 2b**, the box is composed of the first perforated panel, the first frame, the second perforated panel, the second frame, and a bottom panel. Each perforated panel has a side length of a and a thickness of w, and is provided with four small holes at an equal interval of b. Below each hole of the first perforated panel, a short duct is coaxially attached. Through each hole of the second perforated panel, a long duct is coaxially inserted. Each duct has an inner diameter equal to that of the corresponding hole.

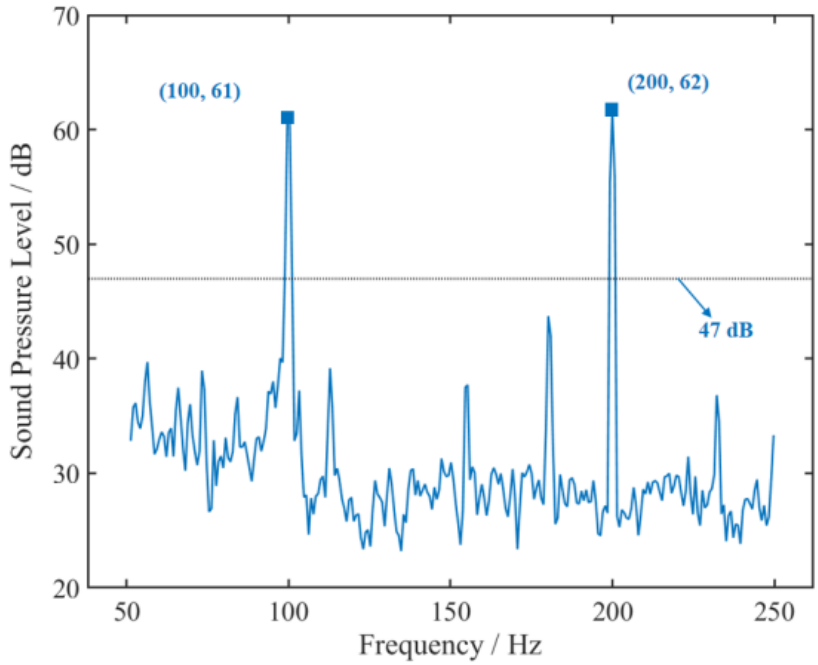

Figure 1. A typical noise spectrum of a 110 kV transformer.

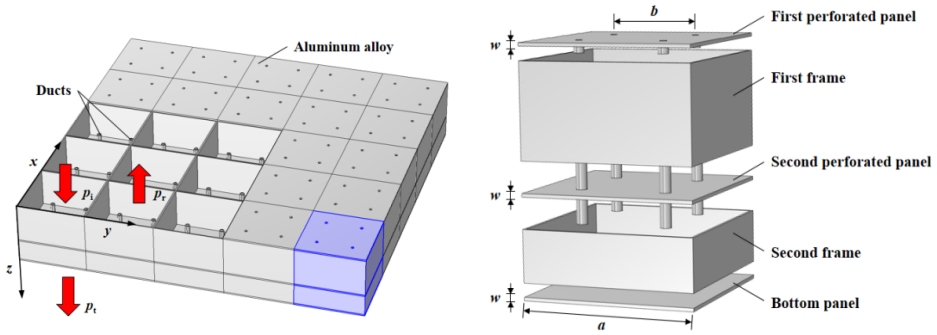

(a) **(b)**

Figure 2. The schematic diagram of SAS. **(a)** An overall view; **(b)** The assembly diagram of the square sound absorption box.

The introduction of an inserted duct can increase the acoustic resistance of the structure and the thermoviscous loss of sound waves in the Helmholtz resonance cavity [22, 23]. Without changing the cavity depth, the acoustic impedance of the Helmholtz resonance cavity can be flexibly adjusted by changing the length of the inserted duct. Thus, the sound absorption peak frequency can be precisely controlled [24, 25]. By vertically coupling two resonant cavities, second-order resonance is generated, which can effectively absorb sound energy at two distinct

frequencies [20,26–30].

2.2. Theoretical model

In order to establish the theoretical model of SAS, appropriate assumptions and simplifications for the basic sound absorption unit were made. The simplified model of SAS is shown in **Figure 3**. Since the first-order resonant frequency of the aluminum alloy panel of SAS is much higher than the target sound wave frequency [31], the vibration of the aluminum alloy panel is relatively weak. Thus, the aluminum alloy panel can be roughly regarded as a rigid surface. Furthermore, each basic unit can be regarded as a serially connected double-layer resonator. Each resonator consists of a duct (denoted as D_i) and a cavity. The duct has a length of l_i and a diameter of d_i. The cavity has a depth of h_i and a cross-sectional area of S. The subscript i of all variables indicates the number of the resonator, and i takes 1 and 2, which corresponds to the first- and second-layer resonators, respectively. Due to the presence of ducts, the shape of the cavities is irregular. Original cavities are partitioned into five sub-cavities by taking end sections of ducts as dividing planes (see **Figure 3**). These five sub-cavities are denoted as C_1 to C_5 from top to bottom.

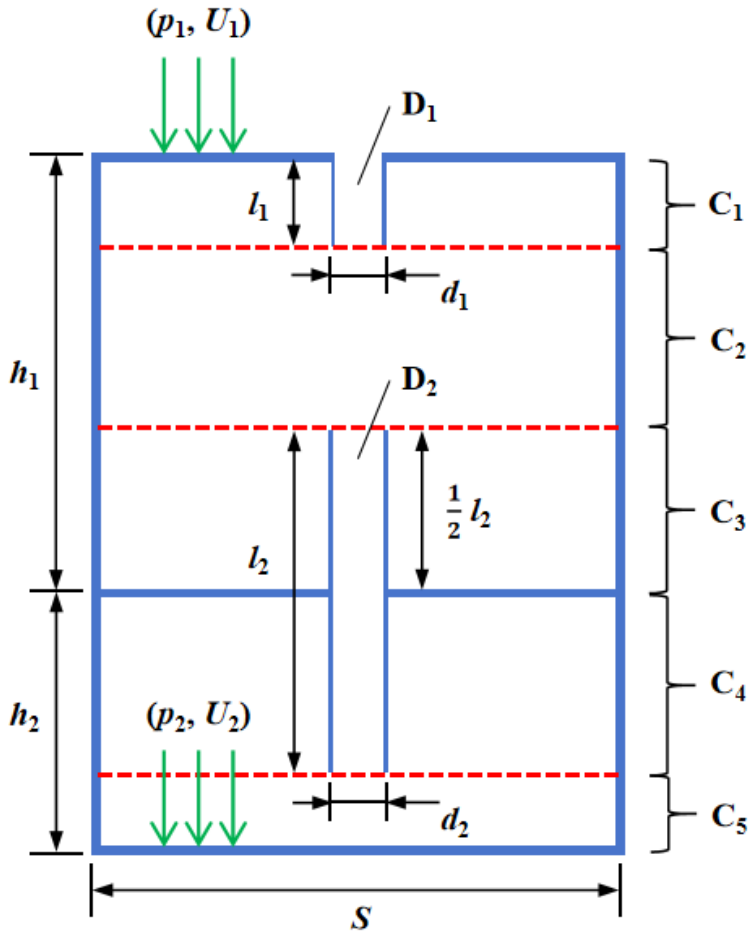

Figure 3. The simplified model of SAS.

According to the assumptions and simplifications above, the sound absorption

coefficient of SAS in a normal incident sound field can be calculated by Equation (1).

$$\alpha = 1 - \left| \frac{Z_{\mathrm{S}} - Z_0}{Z_{\mathrm{S}} + Z_0} \right| \tag{1}$$

where $Z_0 = \rho_0 c_0$, ρ_0 and c_0 are the density and sound speed of air, respectively. Z_{S} is the surface acoustic impedance and can be calculated by the transfer matrix method [32].

Denote the transfer matrix of the duct of the *i*-th layer as $T_{\mathrm{D}i}$ and let those of sub-cavities from top to bottom as T_{C1} to T_{C5}. The relationship between acoustic parameters of the first perforated panel (surface sound pressure p_1 and volume velocity U_1) and the bottom panel (surface sound pressure p_2 and volume velocity U_2) can be expressed as Equation (2).

$$\begin{bmatrix} p_1 \\ U_1 \end{bmatrix} = T_{\mathrm{D1}} T_{\mathrm{C1}} T_{\mathrm{C2}} T_{\mathrm{C3}} T_{\mathrm{D2}} T_{\mathrm{C4}} T_{\mathrm{C5}} \begin{bmatrix} p_2 \\ U_2 \end{bmatrix} \tag{2}$$

The transfer matrix of the duct $T_{\mathrm{D}i}$ can be expressed as Equation (3).

$$T_{\mathrm{D}i} = \begin{bmatrix} 1 & Z_{\mathrm{D}i} \\ 0 & 1 \end{bmatrix} \tag{3}$$

where $Z_{\mathrm{D}i}$ is the acoustic impedance of the duct, defined as the ratio of sound pressure difference between both ends of the duct to the average volume velocity of air inside the duct. Let the duct be parallel to the *z*-axis. Then the sound pressure $p(z)$ and particle velocity $v(z)$ of air along the *z*-axis inside the duct can be calculated by Equation (4).

$$p(z) = pe^{-jk^e z}, v(z) = ve^{-jk^e z} \tag{4}$$

where k^e is the equivalent wave number of air in the duct. Since duct length is much smaller than the acoustic wavelength, the average air velocity in the duct is approximately equal to the air velocity at the center of the duct. Thus, $Z_{\mathrm{D}i}$ can can be calculated by Equation (5).

$$Z_{\mathrm{D}i} = -\frac{2jZ_i^e}{S_i} \sin\left(\frac{k_i^e \mathrm{l}_i}{2}\right) \tag{5}$$

where $S_i = \pi {d_i}^2 / 4$ and $Z_i^e = \rho_i^e \omega / k_i^e$ are the cross-sectional area of the duct of *i*-th layer and the acoustic impedance ratio of air in the duct, respectively. ω is the angular frequency of sound. ρ_i^e and k_i^e are the equivalent density and equivalent wave number of air in the duct, respectively. Due to the thermoviscous loss in the duct, ρ_i^e and k_i^e can be calculated by Equation (6) [24].

$$\rho_i^e = \frac{\rho_0}{\Psi_{\mathrm{v}i}}, k_i^e = k_0 \sqrt{\frac{\gamma - (\gamma - 1)\Psi_{\mathrm{h}i}}{\Psi_{\mathrm{v}i}}} \tag{6}$$

where $\Psi_{\mathrm{h}i}$ and $\Psi_{\mathrm{v}i}$ are functions of thermal field and viscosity field, respectively, and

can be calculated by Equation (7) [33].

$$\Psi_{\mathrm{h}i} = \frac{J_2\left(k_{\mathrm{h}} d_i/2\right)}{J_0\left(k_{\mathrm{h}} d_i/2\right)},\ \Psi_{\mathrm{v}i} = \frac{J_2\left(k_{\mathrm{v}} d_i/2\right)}{J_0\left(k_{\mathrm{v}} d_i/2\right)} \tag{7}$$

where J_n, k_{h}, and k_{v} are the Bessel function of the first kind of order *n*, thermal wave number, and viscous wave number, respectively. Since thicknesses of thermal boundary layer and viscous boundary layer are much smaller than acoustic wavelength, k_{h} and k_{v} can be calculated by Equation (8).

$$k_{\mathrm{h}}{}^2 = -j\omega\frac{\rho_0 C_{\mathrm{p}}}{\kappa}, k_{\mathrm{v}}{}^2 = -j\omega\frac{\rho_0}{\eta} \tag{8}$$

where C_{p}, κ, and η are the isobaric specific heat capacity, thermal conductivity, and kinematic viscosity of air, respectively.

If the acoustic radiation of the duct is considered, an end impedance will be introduced [34]. In addition, the friction of air near the duct wall should be considered. After correction, $Z_{\mathrm{D}i}$ can can be calculated by Equation (9).

$$Z_{\mathrm{D}i} = \frac{1}{S_i}\left\{-\frac{2j\rho_0 c_0 \sin\left(\frac{k_i^e l_i}{2}\right)}{\sqrt{\left[\gamma-(\gamma-1)\Psi_{\mathrm{h}i}\right]\Psi_{\mathrm{v}i}}} + j\omega\rho_0\delta_i + 2\sqrt{2\omega\rho_0\eta}\right\} \tag{9}$$

where $j\omega\rho_0\delta_i$ and $2\sqrt{2\omega\rho_0\eta}$ are corresponding to the end impedance and the friction loss, respectively. δ_i can be calculated by Equation (10).

$$\delta_i = \left[1+(1-1.25\varepsilon_i)\right]\times(4/3\pi)\, d_i \tag{10}$$

where $\varepsilon_i = S_i/S$, S_i is the cross-sectional area of the duct of *i*-th layer, S is the cross-sectional area of the sub-cavity.

The transfer matrix of sub-cavity C_1 can be calculated by Equation (11).

$$T_{\mathrm{C1}} = \begin{bmatrix} 1 & 0 \\ 1/Z_{\mathrm{C1}} & 1 \end{bmatrix} \tag{11}$$

where Z_{C1} is the acoustic impedance of sub-cavity C_1. When there is no duct, Z_{C1} can be calculated by Equation (12).

$$Z_{\mathrm{C1}} = -j\rho_0 c_0 \cot(k_0 l_1)/S \tag{12}$$

Due to the presence of duct D_1, the shape of sub-cavity C_1 is irregular, and its acoustic impedance needs to be corrected. After correction, Z_{C1} can be calculated by Equation (13).

$$Z_{\mathrm{C1}} = -j\rho_0 c_0{}^2/(\omega V_1) \tag{13}$$

where $V_1 = (S - S_1)\, l_1$ is the actual volume of sub-cavity C_1.

Transfer matrices and acoustic impedance of sub-cavities C_3 and C_4 can be calculated in the same way as those of sub-cavity C_1, with parameters replaced by those corresponding to C_3 and C_4, as shown in Equations (11) and (13).

Transfer matrices of sub-cavities C_2 and C_5 can be calculated by Equations (14) and (15), respectively [28].

$$T_{C2} = \begin{bmatrix} \cos\left[k_0\left(h_1 - l_1 - l_2/2\right)\right] & j\sin[k_0\left(h_1 - l_1 - l_2/2\right)]\, Z_0/S \\ j\sin[k_0\left(h_1 - l_1 - l_2/2\right)]\, S/Z_0 & \cos\left[k_0\left(h_1 - l_1 - l_2/2\right)\right] \end{bmatrix} \tag{14}$$

$$T_{C5} = \begin{bmatrix} \cos\left[k_0\left(h_2 - l_2/2\right)\right] & j\sin[k_0\left(h_2 - l_2/2\right)]\, Z_0/S \\ j\sin[k_0\left(h_2 - l_2/2\right)]\, S/Z_0 & \cos\left[k_0\left(h_2 - l_2/2\right)\right] \end{bmatrix} \tag{15}$$

Since the bottom panel is a rigid surface, its volume velocity $U_2 = 0$. Substitute U_2 into Equation (2) and the surface acoustic impedance Z_S can can be calculated by Equation (16).

$$Z_S = \frac{p_1}{U_1/S} \tag{16}$$

According to the theory above, the cavity depth, duct length, and duct diameter of the square sound absorption box were quickly optimized using a genetic algorithm. The perforated plate was designed with a side length of 100 mm, a hole interval of 50 mm, and a thickness of 2 mm. Final structural parameters are listed in **Table 1**. According to **Table 1**, the total height of the square sound absorption box is 91 mm.

Table 1. Final structural parameters of a square sound absorption box.

Structural parameters	Values (mm)
a	100
b	50
w	2
h_1	55
h_2	30
l_1	7
l_2	37
d_1	4
d_2	4.5

3. Numerical simulation of SAS

3.1. Numerical model

The finite element software COMSOL Multiphysics 6.2 was used for numerical simulation. The numerical model of SAS is shown in **Figure 4**. According to **Figure 4**, the numerical model contains a square sound absorption box, and its geometric dimensions are consistent with the structural parameters listed in **Table 1**. Air domains inside ducts were modeled with the Thermoviscous Acoustics Module, and the rest were modeled with the Pressure Acoustics Module. The first perforated panel, the first frame, the second perforated panel, the second frame, and the bottom panel were modeled with the Solid Mechanics Module. Perfectly matched layers (PML) were applied at both ends of the numerical model to eliminate the interference of reflected sound. In addition, Floquet periodic boundary conditions were applied to all sides of the numerical model.

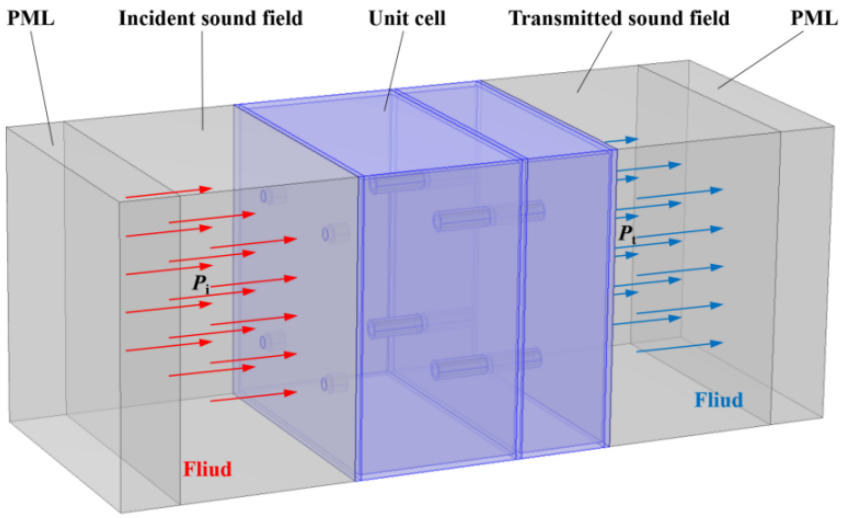

Figure 4. The numerical model of SAS.

3.2. Sound absorption performance and mechanism of SAS

The comparison between the analysis and simulation results of the sound absorption coefficient in the normal incident sound field is shown in **Figure 5a**. According to **Figure 5a**, analytical and simulated calculation results are basically consistent, which indicates that the theoretical model is accurate and reliable. SAS has quasi-perfect sound absorption peaks at 100 Hz and 200 Hz, where sound absorption coefficients both exceed 0.96. According to the theoretical model, the normalized surface acoustic impedance of SAS was calculated to clarify the sound absorption mechanism, as shown in **Figure 5b**. According to **Figure 5b**, the normalized acoustic resistance $\mathrm{Re}\left(Z_S/Z_0\right)$ of SAS is approximately 0.9 at 100 Hz and 1.1 at 200 Hz, while the normalized acoustic reactance $\mathrm{Im}\left(Z_S/Z_0\right)$ of SAS is close to zero at both frequencies. These results indicate that the acoustic impedance of SAS is dominated by the real part and is basically matched with the acoustic impedance of air at resonant frequencies. Proper impedance matching indicates that the majority of incident sound energy can enter the structure. The sound pressure level and the particle velocity of air inside SAS at resonant frequencies are shown in **Figure 5c,d**, respectively. **Figure 5c,d** indicates that the incident sound energy at 100 Hz and 200 Hz is trapped inside ducts and cavities and dissipates through the resonance of the structure.

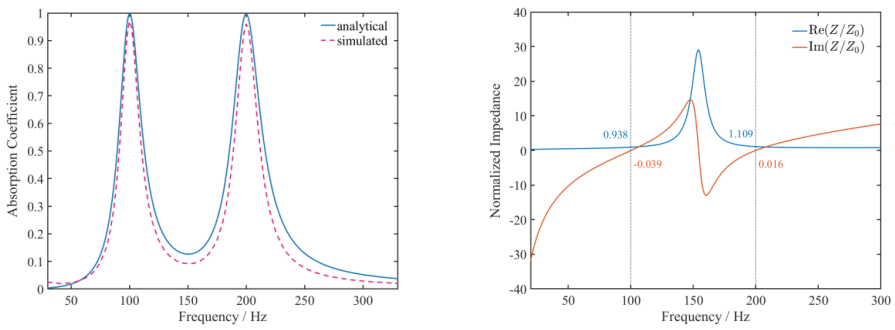

(a) **(b)**

Figure 5. *Cont.*

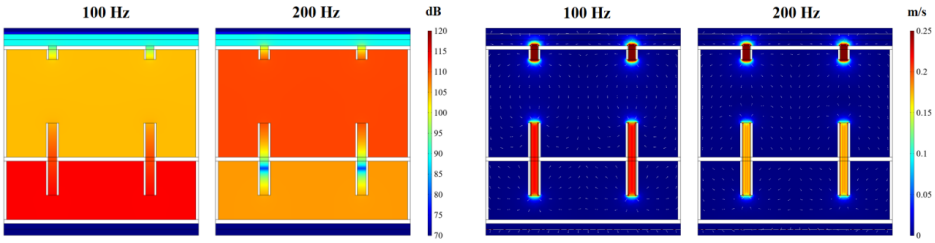

(c) **(d)**

Figure 5. Acoustic characteristics of SAS in the normal incident sound field. **(a)** Sound absorption coefficient; **(b)** Normalized surface acoustic impedance; **(c)** The distribution of sound pressure level; **(d)** The distribution of the particle velocity of air.

According to Equations (2)–(16) in Section 2.2, acoustic impedance and duct length satisfy a nonlinear functional relationship. To visualize this relationship, curves of normalized acoustic impedance Z/Z_0 versus duct length l_1 and l_2 are shown in **Figure 6**. As shown in **Figure 6**, the precise control of the acoustic impedance can be achieved by adjusting the duct length.

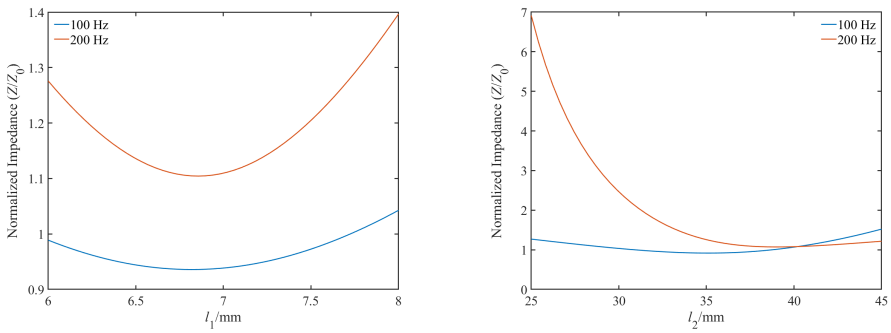

(a) **(b)**

Figure 6. The effect of duct length on the normalized impedance of SAS. **(a)** Normalized impedance versus l_1 for different frequencies; **(b)** Normalized impedance versus l_2 for different frequencies.

The results and discussions above are based on the case of normal incidence. Since sound waves arrive from random directions in practical applications, the sound absorption performance of SAS in a diffuse sound field was further studied by numerical simulation. Sound absorption coefficient in an ideal diffuse sound field can be defined as the average of oblique sound absorption coefficients over elevation angle θ and azimuth angle φ, as given in Equation (17) [35].

$$\alpha_{\text{diff}} = \frac{\int_0^{2\pi}\int_0^{\theta_{\text{lim}}} \alpha(\varphi,\theta)\sin\theta\cos\theta \mathrm{d}\theta\mathrm{d}\varphi}{\int_0^{2\pi}\int_0^{\theta_{\text{lim}}} \sin\theta\cos\theta \mathrm{d}\theta\mathrm{d}\varphi} \tag{17}$$

where θ_{lim} is the upper limit of elevation angle, above which no sound is assumed to be incident on the structure. Generally, θ_{lim} ranges from 70° to 85° in laboratory conditions [36]. To facilitate numerical calculations, θ_{lim} was taken as 75° in this study [37]. $\alpha(\varphi,\theta)$ is the sound absorption coefficient of SAS excited by a sound wave with azimuth angle φ and elevation angle θ, and it was calculated by the numerical model. The sound absorption coefficient of SAS in the diffuse sound field is shown in

Figure 7. According to **Figure 7**, resonant frequencies remain unchanged in the case of random incidence. Compared with those in the normal incidence sound field, sound absorption coefficients in the diffuse sound field are slightly reduced, but still maintain high values of 0.85 at 100 Hz and 0.84 at 200 Hz.

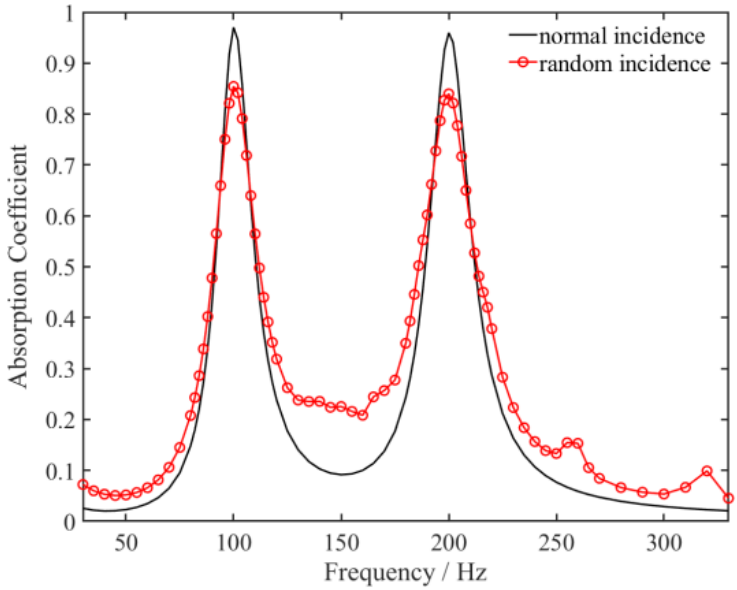

Figure 7. The simulation result of the sound absorption coefficient in the diffuse sound field.

Table 2 compares performance differences between the SAS in this study and other sound absorption structures. This study fabricated a dual-layer Helmholtz resonator (HR) equipped with inserted ducts through machining, which can efficiently absorb sound energy of 100 Hz and 200 Hz at a thickness of 91 mm. Liang et al. [30] and Ji et al. [37] reported sound absorption structures that can absorb sound energy of 100–400 Hz and 50–100 Hz, respectively. Their sound absorption coefficients are close to SAS's, but their structural thicknesses are about twice SAS's. Sharafkhani [21] adopted a vertically nested triple-layer Helmholtz resonator. Its sound absorption coefficient at normal incidence is close to that of SAS, and its structural thickness is about half that of SAS. However, its spatial structure is complex and suitable for 3D-printing, which results in high actual production costs. Using aluminum alloy panels and pipes, SAS can be manufactured through simple machining (see **Figure 8**). Thus, the production cost of SAS is low. Moreover, the inserted duct of SAS in this study is obviously different from those of sound absorption structures in the studies by Sharafkhani [21], Liang et al. [30], and Ji et al. [37]. The inserted duct located on the intermediate partition of SAS runs through the intermediate partition and occupies both the upper and lower resonator cavities, while inserted ducts of sound absorption structures [21, 30, 37] are located below intermediate partitions and occupy only the lower resonator cavities. This special acoustic structure of SAS changes the acoustic impedance of the upper cavity (see Equations (12)–(14)). Simulation results of the sound absorption coefficient of SAS using the above two types of inserted ducts are shown in **Figure 9**. As shown in **Figure 9**, under the condition of unchanged external dimensions such as the thickness of the sound absorption unit, the design of the duct

penetrating the intermediate partition reduces the first and second resonant frequencies of SAS by about 10 Hz and 30 Hz, respectively. This means that if the resonant sound absorption frequency is the same, the SAS with the duct penetrating the intermediate partition design has a thinner thickness and smaller volume.

Table 2. Performance differences between SAS and other sound absorption structures.

Structure	Range (Hz)	Performance	Thickness (mm)	Fabrication	Ref.
Dual-layer HR + inserted duct	100, 200	$\alpha \geq 0.83$	91	Machining	This study
HR + inserted duct	50–100	$\alpha_{avg} \geq 0.85$	200	3D-printing	Ji et al. [37]
Nested HR + inserted duct	100–400	$\alpha_{avg} \geq 0.8$	182	3D-printing	Liang et al. [30]
Nested HR + inserted duct	100, 200, 300	$\alpha \geq 0.9$	55	3D-printing	Sharafkhani [21]

Note: The sound absorption coefficient of the structure in the research by Sharafkhani [21] is based on the case of normal incidence.

(a) **(b)**

Figure 8. The manufacture of SAS. **(a)** Inserted ducts; **(b)** Cavities equipped with inserted ducts.

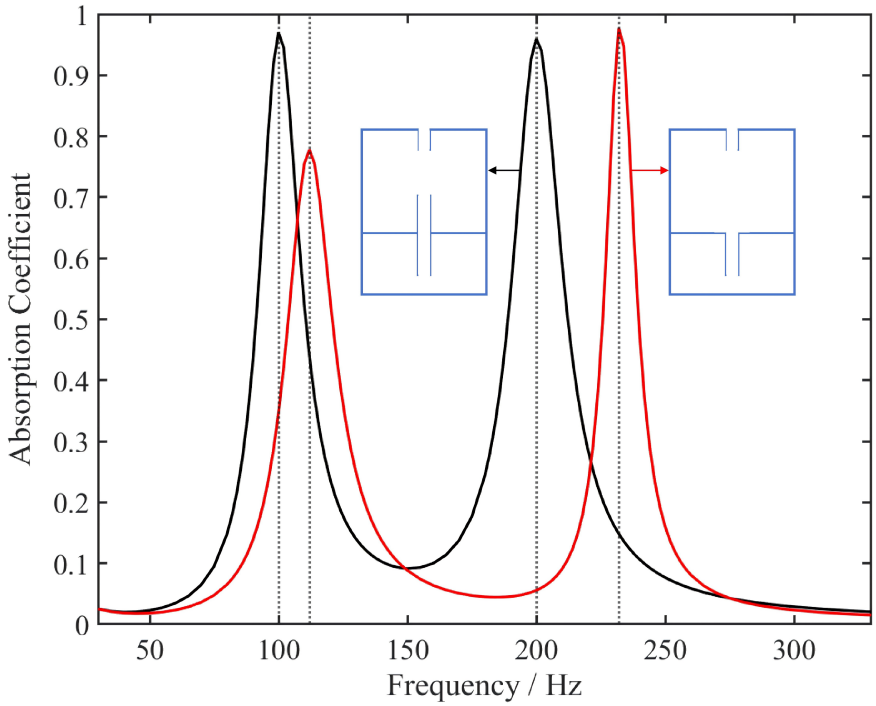

Figure 9. Comparison of sound absorption performance between two types of inserted ducts located on the intermediate partition of SAS.

During the manufacture of SAS samples, there are errors in structural parameters. To analyze the sound absorption frequency drift caused by these errors, the influence of structural parameter uncertainty on SAS sound absorption performance was analyzed through numerical simulation. Results are shown in **Figures 10–12**. **Figure 10** shows that the uncertainty of duct length has little effect on the resonant frequency and its peak absorption coefficient. As shown in **Figure 11**, an increase in the first cavity depth h_1 will cause a decrease in the second resonant frequency, and an increase in the second cavity depth h_2 will cause a decrease in the first resonant frequency. **Figure 12** indicates that an increase in the duct diameter will lead to an increase in the second resonant frequency. Structural parameter errors caused by machining usually follow a normal distribution. By introducing random errors that follow a normal distribution to l_1, l_2, h_1, h_2, d_1, and d_2 simultaneously, the robustness of the sound absorption performance of SAS was further analyzed. According to l_1, l_2, h_1, h_2, d_1, and d_2 given in **Table 1**, assuming that standard deviations of these structural parameters caused by machining are all σ, three standard deviation levels were set in combination with the accuracy of aluminum alloy processing, namely σ = 0.1 mm, 0.2 mm, and 0.3 mm. 10,000 sets of structural parameters were randomly generated for each standard deviation σ. According to the theoretical model in Section 2.2, changes in sound absorption coefficients caused by structural parameter errors were statistically analyzed (see **Figure 13**). The blue solid line in **Figure 13** represents the sound absorption coefficient calculated according to the parameters given in **Table 1**. The blue dashed line represents the mean value of the sound absorption coefficient calculated according to 10,000 sets of structural parameters. The pink circle represents the mean absolute error of the sound absorption coefficient calculated according to 10,000 sets of structural parameters. As shown in **Figure 13**, resonant frequencies of SAS remain unchanged, and peak absorption coefficients decrease after introducing standard deviations. However, the maximum decrement of peak absorption coefficients does not exceed 22.2%. **Table 3** calculates standard deviations and confidence intervals of the SAS absorption coefficient at 100 Hz and 200 Hz under worst-case conditions (σ = 0.3 mm). As shown in **Table 3**, the mean value of the absorption coefficient at 100 Hz is 0.870, the standard deviation is 0.139, and the 95% confidence interval is (0.867, 0.873). The mean value of the absorption coefficient at 200 Hz is 0.776, the standard deviation is 0.197, and the 95% confidence interval is (0.772, 0.780). The widths of 95% confidence intervals of the absorption coefficient at 100 Hz and 200 Hz are narrow, which indicates that the deviation of the absorption coefficient caused by the worst-case scenario is not significant. In practical engineering applications of SAS, this result can serve as one of the bases for evaluating the reliability of its sound absorption performance under adverse conditions.

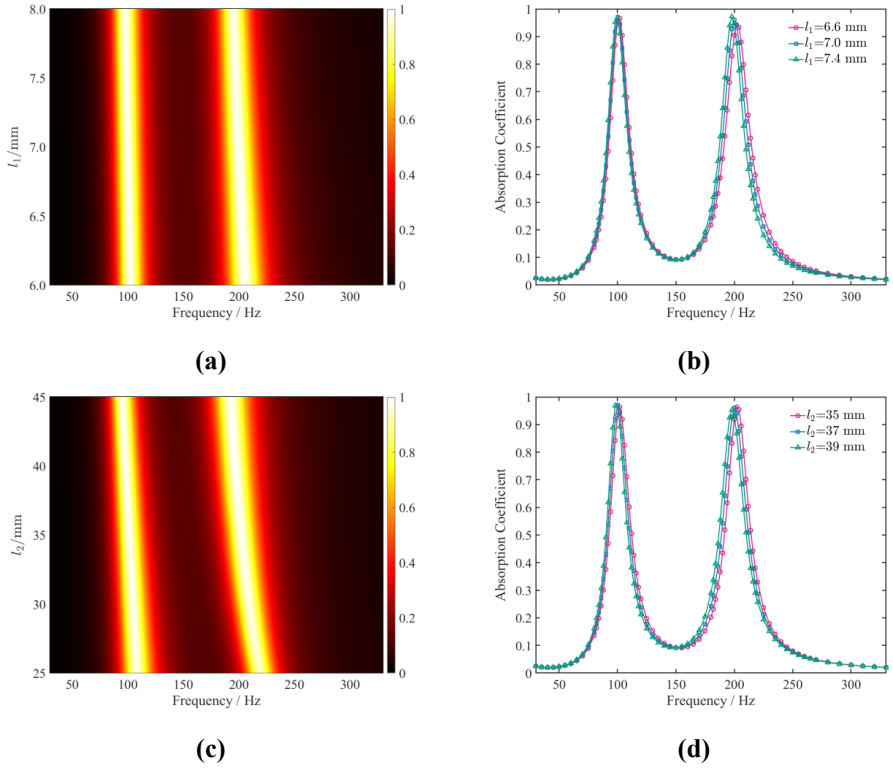

Figure 10. The effect of duct length on the sound absorption performance of SAS. **(a)** Sound absorption spectrum for different l_1; **(b)** Sound absorption coefficient versus frequency for different l_1; **(c)** Sound absorption spectrum for different l_2; **(d)** Sound absorption coefficient versus frequency for different l_2.

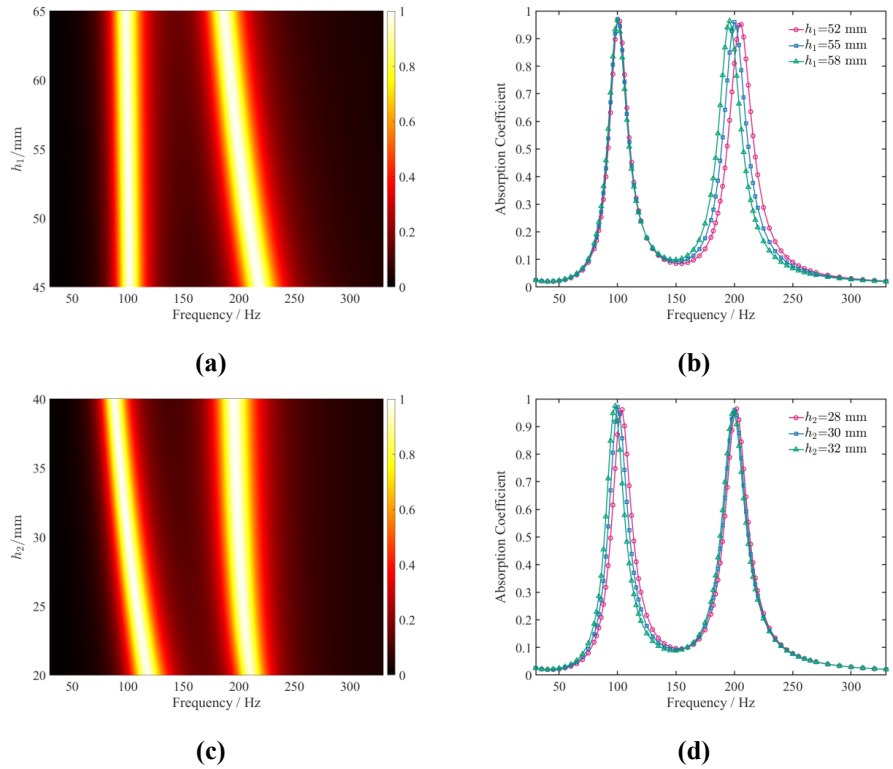

Figure 11. The effect of cavity depth on the sound absorption performance of SAS. **(a)** Sound absorption spectrum for different h_1; **(b)** Sound absorption coefficient versus frequency for different h_1; **(c)** Sound absorption spectrum for different h_2; **(d)** Sound absorption coefficient versus frequency for different h_2.

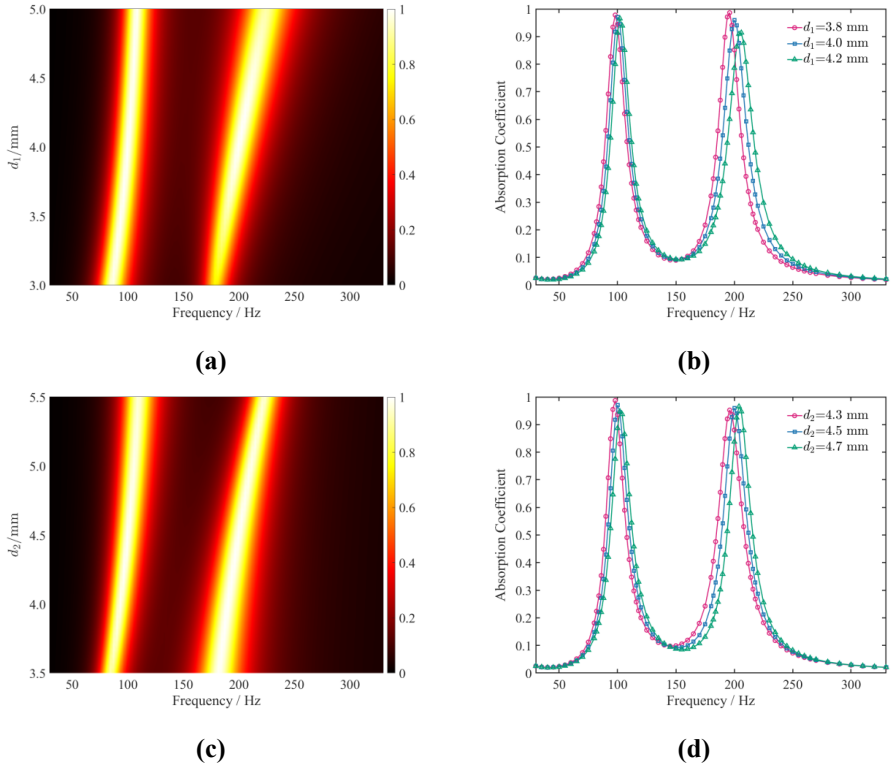

Figure 12. The effect of duct diameter on the sound absorption performance of SAS. **(a)** Sound absorption spectrum for different d_1; **(b)** Sound absorption coefficient versus frequency for different d_1; **(c)** Sound absorption spectrum for different d_2; **(d)** Sound absorption coefficient versus frequency for different d_2.

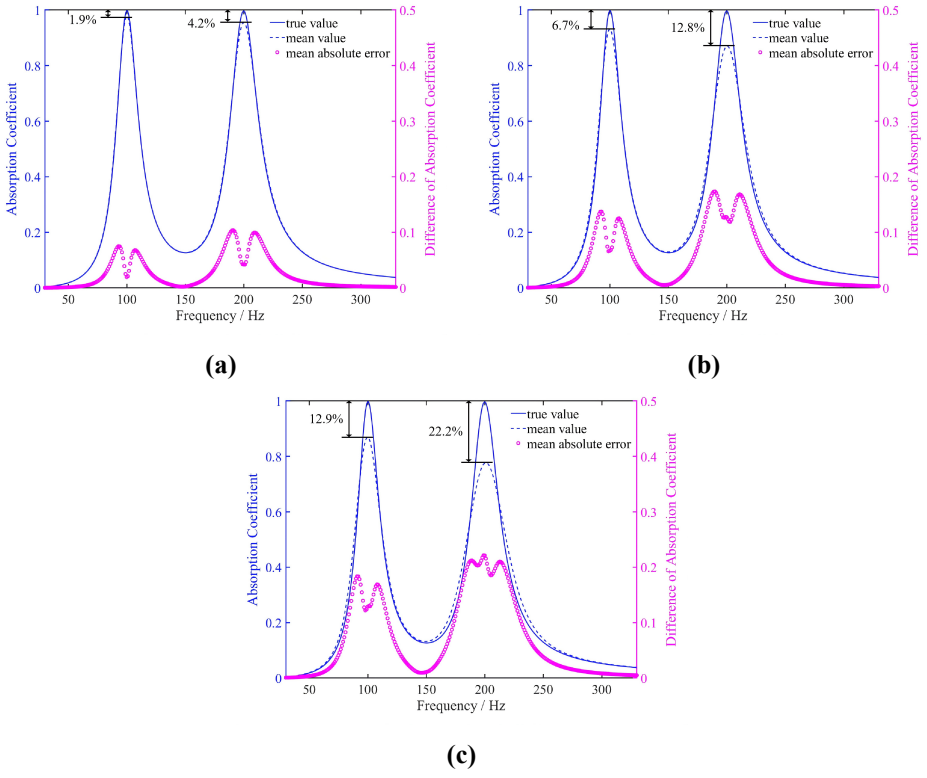

Figure 13. The robustness of the sound absorption performance of SAS after introducing different standard deviations. **(a)** σ = 0.1 mm; **(b)** σ = 0.2 mm; **(c)** σ = 0.3 mm.

Table 3. Standard deviations and confidence intervals of sound absorption coefficient after introducing structural parameter errors under worst-case conditions.

Frequency (Hz)	Absorption coefficient		
	Mean values	Standard deviations	Confidence intervals (α = 0.05)
100	0.870	0.139	(0.867, 0.873)
200	0.776	0.197	(0.772, 0.780)

4. Experimental research of SAS

4.1. Sound absorption performance measurement

According to ISO 10534-2:2023, the transfer function method was used to measure the sound absorption coefficient of SAS in a normal incident sound field. Experimental equipment included a power amplifier, an impedance tube, a speaker, two microphones, a data acquisition card, and a laptop computer. Since the cutoff frequency of sound waves in an impedance tube is related to its cross-sectional dimensions, an impedance tube with the cross section of 101 mm × 101 mm was selected to cover the main sound absorption frequency band. In order to improve measurement accuracy, the exchange channel method was applied to further eliminate measurement errors caused by the phase difference between microphones. **Figure 14** shows an actual sample of the square sound absorption box of SAS used for impedance tube testing. A comparison between experiment and simulation results in the normal incident sound field is shown in **Figure 15**. According to **Figure 15**, measured values of sound absorption coefficient in the normal incident sound field reach 0.93 at 100 Hz and 0.90 at 200 Hz, and are in good agreement with simulated values. The measured absorption coefficient of SAS on the non-design frequency band is relatively low, but exceeds 0.1.

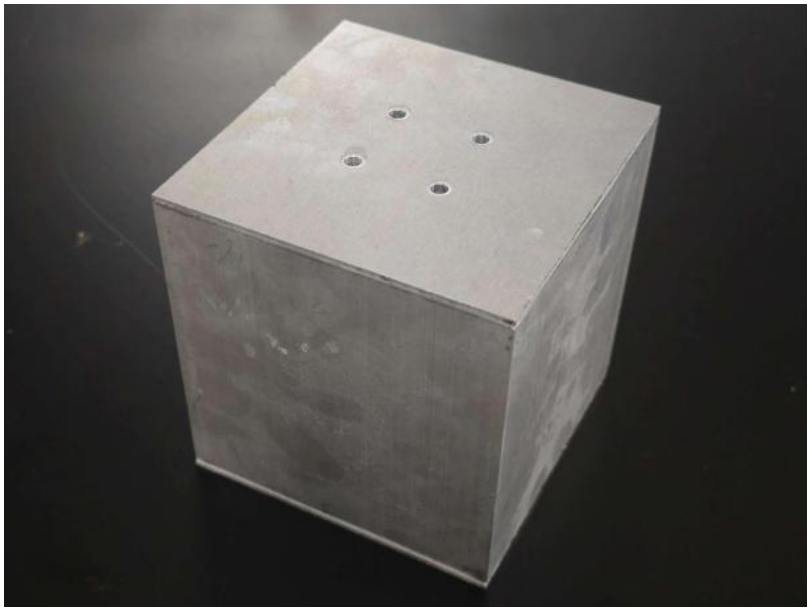

Figure 14. An actual sample of the square sound absorption box of SAS used for impedance tube testing.

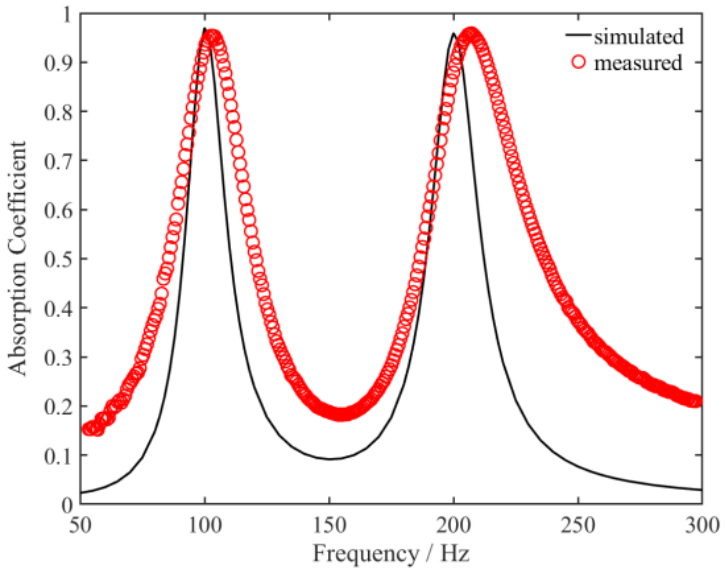

Figure 15. The comparison between experiment and simulation results in the normal incident sound field.

According to ISO 354:2003, the reverberation chamber method was used to measure the sound absorption coefficient of SAS in a diffuse sound field. The test sample consisted of 10 sound absorption panels, and each panel had a size of 1000 mm (length) × 1000 mm (width) × 91 mm (height) which contained 100 square sound absorption boxes (see **Figure 16**). Experiment results of the sound absorption coefficient in the diffuse sound field are listed in **Table 4**. According to **Table 4**, measured values of the sound absorption coefficient of SAS reach 0.83 at 100 Hz and 0.88 at 200 Hz. Absolute errors between measured and simulated values are 0.02 and 0.04, respectively. These results indicate that SAS has excellent sound absorption performance at the interested frequencies in the diffuse sound field.

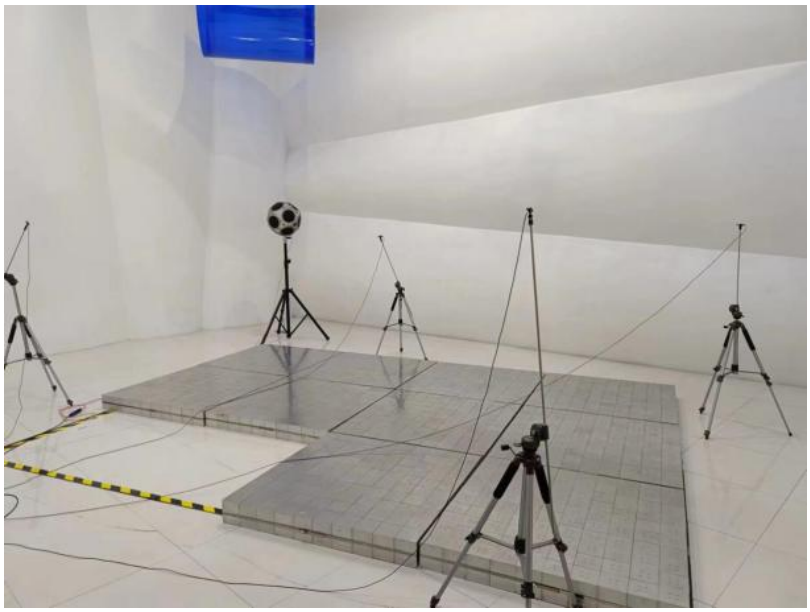

Figure 16. Measuring the sound absorption coefficient of SAS in a diffuse sound field using the reverberation chamber method.

Table 4. The comparison between experiment and simulation results in the diffuse sound field.

Frequency (Hz)	Absorption coefficient			
	Before fire and weather resistance tests			After fire and weather resistance tests
	Measured values	Simulated values	Absolute errors	Measured values
100	0.83	0.85	0.02	0.81
200	0.88	0.84	0.04	0.85

4.2. Fire resistance and weather resistance tests

According to EN 13501-1:2007, ISO 4892-3:2024, ISO 17223:2014, ASTM D5510-94, and ASTM D2243-95, the fire resistance and weather resistance of SAS were tested, as shown in **Table 5**. According to **Table 5**, the fire resistance grade of SAS reaches the A1 level, which indicates that SAS is completely non-combustible. The aging resistance and freeze-thaw resistance of SAS are excellent as well. These non-acoustic properties make SAS have good engineering application prospects. As listed in **Table 4**, after fire resistance and weather resistance tests, measured values of the sound absorption coefficient of SAS still reach 0.81 at 100 Hz and 0.85 at 200 Hz, which indicates that the sound absorption performance of SAS is not obviously compromised. According to the analysis in Section 3.2, slight changes in the sound absorption coefficient before and after testing may be due to the variation of duct diameter caused by thermal expansion and contraction of the aluminum alloy.

Table 5. The fire resistance and weather resistance of SAS.

Performance	Indices	Criteria	Results
Fire resistance (A1 level)	Temperature rise	≤30 ℃	7 ℃
	Mass loss	≤50%	0
	Duration of sustained flaming	=0 s	0
	Gross calorific potential	≤2.0 MJ/kg	0
Light aging resistance	Appearance change	N/A	No obvious changes
	Yellowness index change	N/A	9.3
Heat aging resistance	Appearance change	N/A	No obvious changes
Freeze-thaw resistance	Appearance change	N/A	No obvious changes

4.3. Installation of SAS

SAS in this study can be made into flat sound absorption panels (see **Figure 16**). These sound absorption panels can be vertically laid on the firewall of the transformer to reduce the impact of low-frequency reflected sound (see **Figure 17a**), or hung on the shell of the transformer through elastic components to reduce the impact of the transformer's direct sound (see **Figure 17b**). The relationship between installation quantity and average sound absorption coefficient is calculated in the scenario where SAS is installed on the firewall (see **Figure 18**). As shown in **Figure 18**, the average sound absorption coefficient approaches 0.8 when the quantity of SAS laid on the firewall reaches 90%.

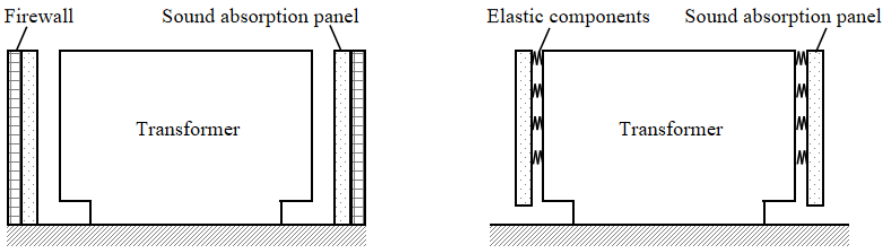

Figure 17. Two installation scenarios of SAS. **(a)** Vertically laid on the firewall of the transformer; **(b)** Hung on the shell of the transformer through elastic components.

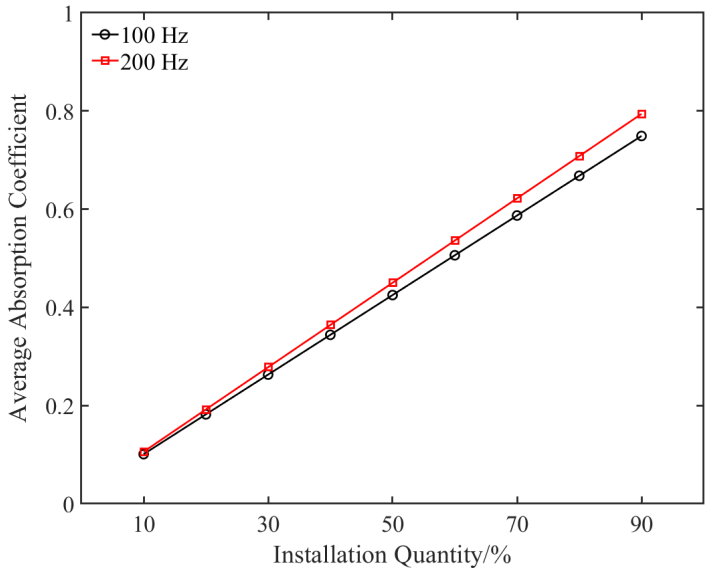

Figure 18. The relationship between the installation quantity of SAS and the average sound absorption coefficient.

4.4. Production cost analysis of SAS

The production cost of SAS is quantitatively analyzed (see **Table 6**). The cost of machining includes material costs and labor costs, while the cost of 3D-printing only includes material costs. The labor cost of machining aluminum alloy materials is approximately 300 CNY/m^2. As shown in **Table 6**, the cost of 3D-printing acrylonitrile butadiene styrene is the lowest, half of that of machining aluminum alloy materials. The cost of 3D-printing ultraviolet-curing resin is slightly higher than machining aluminum alloy materials. According to the analysis in Section 2.2, SAS in this study has high requirements for material fire resistance and weather resistance. Only metal powder meets the requirements among these 3D-printing materials, but its production cost is extremely high.

Table 6. Cost comparison between machining and 3D-printing.

Processing method	Material	Unit price	Total price
Machining	Aluminum alloy	18 CNY/kg	700 CNY/m^2
3D-printing	Acrylonitrile butadiene styrene	40 CNY/kg	350 CNY/m^2
	Ultraviolet curing resin	90 CNY/kg	800 CNY/m^2
	Metal powder	400 CNY/kg	9000 CNY/m^2

5. Conclusion

Regarding material fire resistance, weather resistance, and ease of machine manufacturing as basic constraints, this study constructed a sound absorption structure (SAS) suitable for low-frequency tonal noise in substations. A theoretical calculation model for the sound absorption coefficient of SAS was established, and the impact of structural parameter uncertainty on SAS's sound absorption performance was simulated and analyzed. Measurement results verified the SAS's excellent low-frequency sound absorption performance. Its sound absorption mechanism was revealed based on impedance matching theory. Results showed sound absorption coefficients at 100 Hz and 200 Hz respectively, reached 0.93 and 0.90 in the normal incident sound field, reached 0.83 and 0.88 in the diffuse sound field. Moreover, the fire resistance grade of SAS reached A1 level, which indicated it was completely non-combustible. Laying SAS on reflective surfaces of structures such as transformer firewalls can reduce the impact of low-frequency noise. Future work can combine SAS engineering applications to measure the sound absorption and noise reduction in different scenarios.

Author contributions: Conceptualization, QL and GD; Formal analysis, QL; Investigation, KX, KW, QL, and GD; Methodology, QL and GD; Supervision, GD; Writing—original draft, KX; Writing—review and editing, KX, KW, QL, and GD. All authors have read and agreed to the published version of the manuscript.

Funding: This work was funded by China Power Engineering Consulting Group Concentrated R&D Projects of Science and Technology (Project No. DG2-P06-2022).

Institutional review board statement: Not applicable.

Informed consent statement: Not applicable.

Data availability statement: The data used to support the findings of this study are available from the corresponding author upon request.

Conflict of interest: The authors declare no conflict of interest.

References

1. Miao XH, Jiang P, Pang FZ, et al. Numerical analysis and experimental research of vibration and noise characteristics of oil-immersed power transformers. Applied Acoustics. 2023; 203: 109189. doi: 10.1016/j.apacoust.2022.109189
2. Di GQ, Chen XW, Song K, et al. Improvement of Zwicker's psychoacoustic annoyance model aiming at tonal noises. Applied Acoustics. 2016; 105: 164–170. doi: 10.1016/j.apacoust.2015.12.006
3. Joseph P, Chaitanya P, Elliott S, et al. Propeller tonal noise reductions through synchrophasing: Mechanisms and performance. Journal of Sound and Vibration. 2025; 610: 119110. doi: 10.1016/j.jsv.2025.119110

4. van den Berg F, Koppen E, Boon J, et al. Sound power of onshore wind turbines and its spectral distribution. Sound and Vibration. 2025; 59: 1716. doi: 10.59400/sv1716
5. Liu QC, Yu WJ, Cheng G. Adaptive narrowband compensation algorithm for active control of the pressure pulsation line spectrum in a liquid pipeline system. Shock and Vibration. 2025; 2025: 9079090. doi: 10.1155/vib/9079090
6. Li H, Chen KA, Li H, et al. Annoyance suppression effect of narrow-band color noises and water sounds on low-frequency tonal noise. Acoustics Australia. 2024; 52: 41–55. doi: 10.1007/s40857-023-00312-w
7. Doleschal F, Verhey JL. Pleasantness and magnitude of tonal content of electric vehicle interior sounds containing subharmonics. Applied Acoustics. 2022; 185: 108442. doi: 10.1016/j.apacoust.2021.108442
8. Azuma D, Hasegawa R. Audible noise from amorphous metal and silicon steel-based transformer core. IEEE Transactions on Magnetics. 2008; 44: 4104–4106. doi: 10.1109/TMAG.2008.2003174
9. Chaitanya P, Joseph P, Narayanan S, et al. Performance and mechanism of sinusoidal leading edge serrations for the reduction of turbulence-aerofoil interaction noise. Journal of Fluid Mechanics. 2017; 818: 435–464. doi: 10.1017/jfm.2017.141
10. Khamis M, Zhang S, Ibrahim S. A Synchronized Filter-s Least Mean Square (SFsLMS) algorithm for multi-channel ANC in aviation noise suppression. Applied Acoustics. 2025; 231: 110552. doi: 10.1016/j.apacoust.2025.110552
11. Lee HM, Hua YT, Wang ZM, et al. A review of the application of active noise control technologies on windows: Challenges and limitations. Applied Acoustics. 2021; 174: 107753. doi: 10.1016/j.apacoust.2020.107753
12. Chu YJ, Mak CM, Zhao Y, et al. Performance analysis of a diffusion control method for ANC systems and the network design. Journal of Sound and Vibration. 2020; 475: 115273. doi: 10.1016/j.jsv.2020.115273
13. Kong WM, Zhang J, Liu PQ. Aerodynamic noise simulation of porous medium-coated cylinder: Broadband hump noise mechanism and effects of permeability and pores distribution on tonal noise. Journal of Sound and Vibration. 2025; 607: 119046. doi: 10.1016/j.jsv.2025.119046
14. Kong WF, Fu T. A novel butterfly double-panel metastructure filled with porous materials for broadband low-frequency sound absorption. Journal of Building Engineering. 2024; 97: 110935. doi: 10.1016/j.jobe.2024.110935
15. Ozturk S, Erol H. Acoustic multi-objective optimization of porous media properties of a diesel particulate filter. Sound and Vibration. 2025; 59: 1805. doi: 10.59400/sv1805
16. Wang DZ, Xiao Y, Wang SX, et al. Ultra-broadband sound-absorbing metastructure with Helmholtz resonator and porous material modulation crown. Materials and Design. 2024; 246: 113351. doi: 10.1016/j.matdes.2024.113351
17. Zheng MY, Chen C, Li XD. Ultra-broadband and nonlinear robust sound absorption based on ultra-microperforated panel. Journal of Sound and Vibration. 2024; 575: 118262. doi: 10.1016/j.jsv.2024.118262
18. Li YL, Lin YM, Yao S, et al. Low-frequency broadband sound absorption of the metastructure with extended tube resonators and porous materials. Applied Acoustics. 2024; 217: 109827. doi: 10.1016/j.apacoust.2023.109827
19. Zhang WT, Xin FX. Broadband low-frequency sound absorption via Helmholtz resonators with porous material lining. Journal of Sound and Vibration. 2024; 578: 118330. doi: 10.1016/j.jsv.2024.118330
20. Lin QH, Shi JH, Zhang J, et al. Spectrum-driven acoustic metasurface for broadband noise control. Results in Physics. 2024; 61: 107725. doi: 10.1016/j.rinp.2024.107725
21. Sharafkhani N. A Helmholtz resonator-based acoustic metamaterial for power transformer noise control. Acoustics Australia. 2022; 50: 71–77. doi: 10.1007/s40857-021-00256-z
22. Zhang L, Zhang WT, Xin FX. Broadband low-frequency sound absorption of honeycomb sandwich panels with rough embedded necks. Mechanical Systems and Signal Processing. 2023; 196: 110311. doi: 10.1016/j.ymssp.2023.110311
23. Bi SH, Wang ES, Shen XM, et al. Enhancement of sound absorption performance of Helmholtz resonators by space division and chamber grouping. Applied Acoustics. 2023; 207: 109352. doi: 10.1016/j.apacoust.2023.109352
24. Huang SB, Fang XS, Wang X, et al. Acoustic perfect absorbers via Helmholtz resonators with embedded apertures. The Journal of the Acoustical Society of America. 2019; 145: 254–262. doi: 10.1121/1.5087128
25. Guo JW, Fang Y, Jiang ZY, et al. An investigation on noise attenuation by acoustic liner constructed by Helmholtz resonators with extended necks. Journal of the Acoustical Society of America. 2021; 149: 70–81. doi: 10.1121/10.0002990
26. Shi QQ, Zhang X, Luo L, et al. Viscoelastic material enhancement of underwater sound absorption in higher-order resonators: From low-frequency to ultra-broadband. Physics Letters A. 2024; 525: 129932. doi: 10.1016/j.physleta.2024.129932
27. Zhao YM, Guo ZC, Ye J, et al. 3D Printed multilayer overlapping resonators for low-frequency broadband sound absorption: Mechanism analysis and corresponding modified theoretical method. Virtual and Physical Prototyping. 2025; 20: 1. doi: 10.1080/17452759.2025.2455540

28. Gori P, Guattari C, Evangelisti L, et al. Layered acoustic structures with equally phased elements. Acoustics. 2025; 7: 12. doi: 10.3390/acoustics7010012
29. Fang BW, Feng PC, Zhang R, et al. Low-frequency broadband acoustic metamaterial absorber based on nested resonator and synergistic coupled weak resonances. Engineering Structures. 2024; 319: 118825. doi: 10.1016/j.engstruct.2024.118825
30. Liang MT, Wu HG, Ibarias M, et al. Subwavelength metasurfaces for quasi-omnidirectional broadband sound absorption at low frequencies. Thin-Walled Structures. 2025; 215: 113591. doi: 10.1016/j.tws.2025.113591
31. Leissa AW. The free vibration of rectangular plates. Journal of Sound and Vibration. 1973; 31: 257–293. doi: 10.1016/S0022-460X(73)80371-2
32. Lee DH, Kwon YP. Estimation of the absorption performance of multiple layer perforated panel systems by transfer matrix method. Journal of Sound and Vibration. 2004; 278: 847–860. doi: 10.1016/j.jsv.2003.10.017
33. Stinson MR. The propagation of plane sound waves in narrow and wide circular tubes, and generalization to uniform tubes of arbitrary cross-sectional shape. Journal of the Acoustical Society of America. 1991; 89: 550–558. doi: 10.1121/1.400379
34. Ingard U. On the theory and design of acoustic resonators. Journal of the Acoustical Society of America. 1953; 25: 1037–1061. doi: 10.1121/1.1907235
35. Lin QH, Di GQ. A high-performance sound insulation component for filter capacitors based on coiled-up acoustic metamaterials. Physica Status Solidi A. 2022; 219: 2200125. doi: 10.1002/pssa.202200125
36. Mahjoob MJ, Mohammadi N, Malakooti S. An investigation into the acoustic insulation of triple-layered panels containing Newtonian fluids: Theory and experiment. Applied Acoustics. 2009; 70: 165–171. doi: 10.1016/j.apacoust.2007.12.002
37. Ji J, Li DT, Li Y, et al. Low-frequency broadband acoustic metasurface absorbing panels. Frontiers in Mechanical Engineering. 2020; 6: 586249. doi: 10.3389/fmech.2020.586249